MULTI-OBJECTIVE OPTIMIZATION OF A MULTI-ELEMENT HIGH-LIFT AIRFOIL

L. Soulat*, W. Dridi*, S. Moreau*, A. Fosso-Pouangue*
***GAUS, Université de Sherbrooke, Qc, Canada**
laurent.soulat@usherbrooke.ca; stephane.moreau@usherbrooke.ca

Keywords: *high-lift, optimization, high-order derivation*

Abstract

A complete procedure to study and optimize a multi-element high-lift device is presented and applied to the L1T2 test case. Numerical simulation reveals the importance of the computational domain to correctly capture the potential effects generated by this configuration. A sensitiviy study is performed using a high-order derivation technique. The influences of the geometrical parameters controling the geometry and physical ones characterising the flow are analysed, with a focus on the coupling between parameters. The high-lift is optimized according to two objectives using a genetic algorithm and the structure of the Pareto front is described.

1 Introduction

The design of efficient high-lift systems is very critical for the environmental impact of aircrafts, in terms of payload and fuel consumption, but also in terms of aero-acoustics. Obviously, the high-lift systems should significantly increase the lift of the airfoil at low speed while keeping a relatively low drag in order to reduce the thrust required during take-off and landing phases. From this point of view, the design of a high-lift device is a multi-objective problem with usually conflicting objectives (drag and lift for instance).

The design of such systems is a complex process, because of the multi-element geometry that yields an important number of independent parameters to optimize. As a matter of fact, the optimization of the relative positioning of the distinct elements can be very tedious, even for a very classical three elements configuration (slat, main body and flap): The relative position of the slat and flap with respect to the main wing is defined by at least three parameters corresponding to two translations and one rotation respectively. Physical parameters, such as the flow angle and the flight Mach number are also important, directly accounting for the flight conditions and impacting the positioning optimization. Indeed, a dozen of parameters are very easily necessary and even more when considering the shape of the elements directly. A manual optimization can almost be ruled out at this point; automatic optimization is the only practical solution. Genetic algorithms are one of the best techniques available at the moment to cope with the multi-objective optimization. Yet, they require numerous flow evaluations to converge towards the Pareto front, which can be very time-consuming. They are usually coupled with approximation techniques to provide a fast response. One possible approximation is to extrapolate the flow-fields from a high-order derivation of the flow around a baseline solution. The calculation of the derivatives is performed once and is equivalent to or faster than the calculation of one flow flow-field with a Reynolds Averaged Navier-Stokes (RANS) numerical simulation. The extrapolation based on a reconstruction by a Taylor series expansion is almost instantaneous, providing a noticeable speed-up for the evaluation of configurations around the baseline.

This paper will present the multi-objective

numerical optimization of a canonical multi-element high lift device. This configuration is presented in the first section, as well as the numerical techniques used for the optimization. The computed flow-field is then described and validated in the second section, with a particular attention to the numerical settings. The optimization results are finally presented in the last section.

2 Description of the optimization problem

2.1 High-lift configuration and parameterization

This study focuses on the three-element high-lift L1T2 device. This configuration was thoroughly studied both numerically and experimentally [1, 2], which provides a good starting point for the sensitivity analysis and optimization. Moreover, this geometry is quite representative of actual high-lift devices, with several sharp trailing edges located within the slat- and flap-coves. The baseline configuration studied here is the configuration with both slat and flap fully deployed. The geometrical and aerodynamical characteristics of this baseline configuration are briefly recalled in the following table.

Chord c (retracted form)	0.7635 m
Slat angle (deployed)	25°
Flap angle (deployed)	-20°
Flight Mach number	0.197
Flow angle	+4.01°
Ambiant static temperature	290 °K
Ambiant static pressure	101300 Pa

Table 1 Characteristics of the L1T2 case

The configuration and the corresponding flow are assumed to be two-dimensional, but the optimization process presented here could be extended without any problem to a three-dimensional case. The baseline configuration is represented in figure 1.

The present optimization focuses on the positioning of the slat and flap with respect to the main airfoil (geometrical parameters), and on the flow angle-of-attack and Mach number (flow parameters). The positioning of the slat or the flap is parameterized by two translations in the horizontal and vertical directions, and one rotation. Without precise knowledge of the actual kinematics on such a high lift system, the rotation centers were chosen at the upper trailing edge of the slat, and at the leading edge of the flap. These positions could also be varied to assess the impact of a given kinematics on both the aerodynamic and acoustic performances. The present eight parameters, along with the position of the rotational centers are illustrated in fig. 1. The parameter variations from the baseline configuration are summarized in tab. 2.

Slat trans. x	baseline ± 5mm
Slat trans. y	baseline ± 5mm
Slat rotation	baseline ± 10°
Flap trans. x	baseline ± 10mm
Flap trans. y	baseline ± 10mm
Flap rotation	baseline ± 10°
Flow angle α	1° - 7°
Mach	0.15 - 025

Table 2 Parameter ranges for optimization

The objectives of the L1T2 optimization are to increase the lift, measured with the lift coefficient C_L, and to decrease the drag coefficient C_D.

2.2 Numerical optimization procedure

The optimization process is constructed in three successive phases. In the first phase, the steady flow-field in the baseline configuration is simulated numerically with a classical RANS flow solver. Once the baseline flow-field is known, the derivatives of the flow variables (i.e. the conservative and turbulent variables) are calculated for every parameter of the study with a dedicated solver. The last step is the optimization itself with a genetic algorithm coupled with the previous parameterization and extrapolation technique.

The numerical mesh used through the whole study is presented in fig. 2. The structured mesh has approximately 120000 grid points. Grid refinement yields a y^+ criterion of y^+=5. The

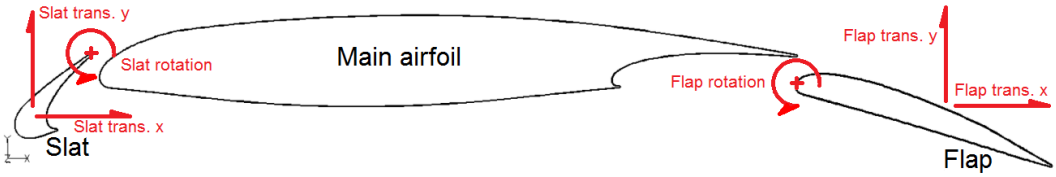

Fig. 1 L1T2 high-lift and positioning parameterization

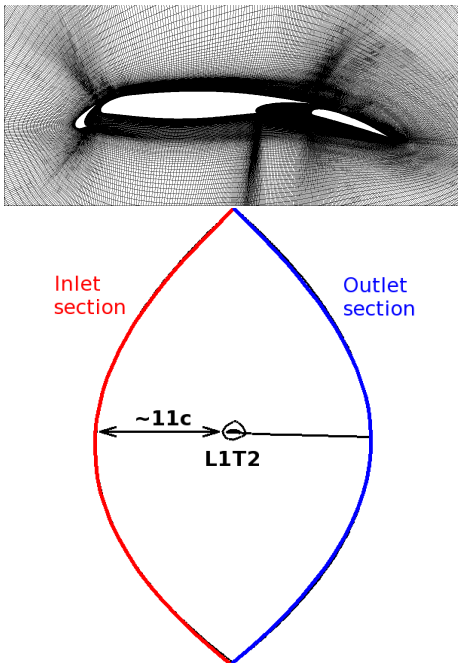

Fig. 2 Mesh configuration

global lens shape was chosen to assure that even for a varying flow angle (up to 60° here), the inlet or outlet boundaries would remain unchanged. Static pressure is imposed at the outlet (right boundary), while density and momentum are set at the inlet. The computational domain is approximately 23c wide in the horizontal direction. The effects of the size of the domain will be discussed later.

2.2.1 Steady flow solver

The baseline configuration was simulated using the finite-volume structured flow solver Turb'Flow developed at Ecole Centrale de Lyon [3]. The steady 2D RANS simulation was performed using a spatial 2^{nd} order centered scheme for the conservative variables, and a 1^{st} order upwind scheme for the turbulent ones. Turbulence was modeled using Kok's two equation k-ω model along with a production limiter for the turbulent kinetic energy. Time discretisation was achieved through an implicit 2^{nd} order scheme with local time stepping. Using these settings, the calculation of the baseline profile requires approximately 20 hours to reach full convergence on a standard workstation.

2.2.2 Parameterization and extrapolation technique

As stated previously, the parameterization technique used in this study relies on the derivation of the flow-field with respect to the parameters. The derivation of the steady Navier-Stokes equation is achieved by the Turb'Opty solver [4]. For this study, the first order, second order and cross derivatives of the flow were calculated. The main advantage of using cross-derivatives is that it allows seeing the coupling effects between the parameters. For the present 8 parameters, this yield 8+8+28=56 derivatives, calculated in 60 h. The extrapolations are achieved with a Taylor series reconstruction. For the current grid, one reconstruction takes about 10 ms. The only limit with such a technique is the truncation error that appears away from the baseline configuration. This error can be easily reduced using higher order derivatives. In the present case with derivatives up to the second order only, the parameter ranges were restricted such that this error was limited to 10%. The corresponding ranges are given in tab. 2.

2.2.3 Optimization technique and post-processing

The optimization was performed using the NSGA-II genetic algorithm [5], modified to in-

clude the previous reconstruction technique instead of direct RANS flow calculation. A 500-individuals population was evolved over 100 generations for the optimization, for a total wall-time of 3 hours on a standard workstation.

To cope with the high-dimensionality of the Pareto-front (8 parameters and two objectives here), the Self-Organizing Maps toolbox [6] is used to post-process the optimization. The main feature of the SOM is to provide as much 2D maps as there are dimensions in the Pareto front but with a unique topology in which one point always corresponds to the same individuals of the Pareto front. The reader can therefore perceive the relationships between the objectives and the parameters on the Pareto front at once.

3 Flow analysis

The overall flow topology and the localflow structures observed on the baseline configuration are quite classical. The flow remains attached over the suction side of all three-elements, although the boundary layer near the trailing edge of the flap is thick. The most noticeable structures are the several vortices located within the slat- and flap-coves and caused by the flow separation at the lower trailing edges of the slat and of the main airfoil (fig. 3, low speed zone in each cove). As expected, the flow emerging from the

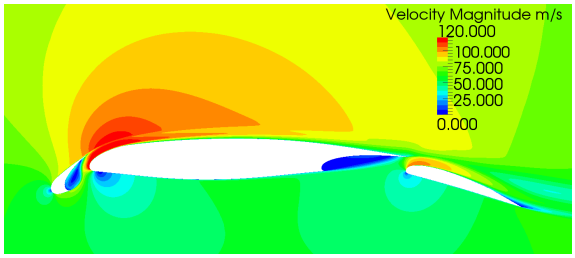

Fig. 3 Velocity magnitude - baseline configuration

coves re-accelerates the boundary layer of the next element, preventing a separation.

3.1 Flow validation

The baseline flow-field computed here is compared with numerical and experimental data available from the literature in terms of pressure coefficient $c_p = \frac{P_s - P_s^\infty}{1/2\rho V_\infty^2}$. As can be seen in fig. 4, the numerical and experimental c_p agree pretty well, except for the slat where a clear discrepancy appears both in terms of average level and shape, and also for the airfoil suction side where the numerical simulation under-predicts the pressure coefficient. This difference can be explained

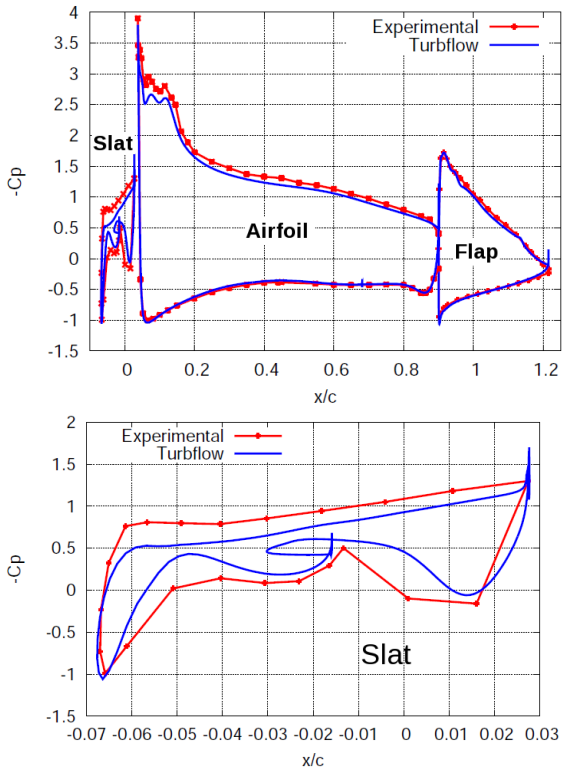

Fig. 4 Baseline configuration : pressure coefficient

by the relatively small size of the computational domain. Two other calculations were performed for the same kind of lens topology, but with an increased inlet (and outlet) distance from the airfoil, up to 55 c and 117 c respectively. When plotting the flow angle along a horizontal line going from the inlet boundary to the slat leading edge, the size of the mesh is seen to have some significant effect (fig. 5).

Indeed, for the smaller $11c$ mesh, the inlet boundary is clearly in the potential zone of the airfoil: the incidence variation for either a 4.01° or a 5° inlet flow angle is not similar to one observed on the large plenum. Consequently, the flow angle imposed on this boundary does

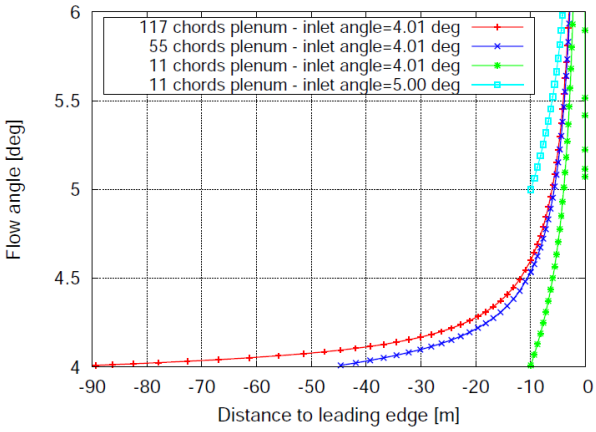

Fig. 5 Flow angle variation - computational domain size effect

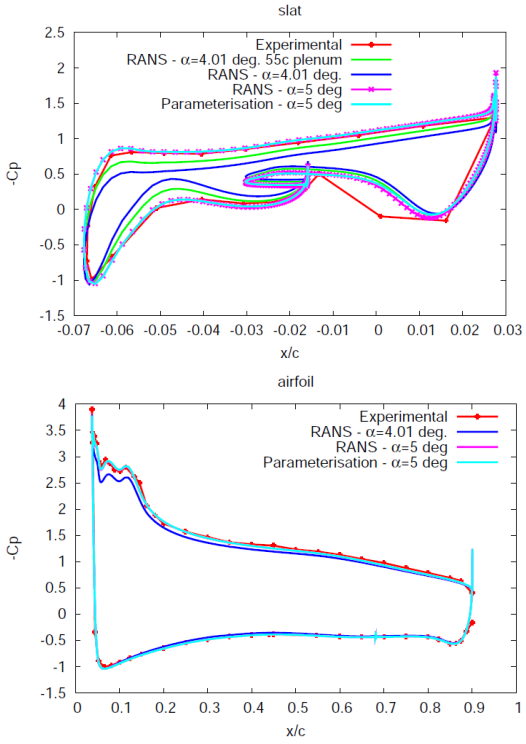

Fig. 6 Flow angle effect on c_p distribution

not correspond to the free-stream value. Given the high camber of the L1T2 (approximately 25+20=45°) yielding a large potential effect, the distance between inlet and airfoil should be at least 50c to ensure a proper simulation of the high flow circulation around the high-lift system.

The second (and coupled) phenomenon causing this difference is the high sensitivity of the slat pressure distribution to the flow angle. This can be measured by comparing the c_p distribution calculated for different flow angles on the 11 c mesh (fig. 6). The sensitivity study is also achieved thanks to the present parameterization technique: the variations induced by the flow angle are reconstructed from the first and second order derivatives with respect to this parameter. The c_p distribution in fig. 6 strongly depends on the flow angle α, particularly for the slat. Indeed, for α=5°, the numerical distribution on the 11 c large grid matches the experimental data very well except in the slat cove, whereas the initial α=4.01° is clearly different. The same trend is observed for the main airfoil. The slat cove flow features are very sensitive to the turbulent model used. Another interesting point is the result of the parameterization. Indeed, the reconstructed solution and the direct RANS calculation at α=5° are almost perfectly superimposed. The only small difference is again within the slat cove, where the parameterization underestimates the pressure coefficient. Since the reconstruction is only based on second order derivatives, this suggests that the flow physics in this region are highly non-linear (third or higher order physics) which is consistent with the presence of the cove vortices at this point. In the end, despite this slight difference, the good agreement between direct RANS calculation and the parameterization technique shows that the latter is valid.

In the following, it was however chosen to keep the 11 c mesh with α=4.01° as a reference to limit the computational cost, when a few calculations of derivatives showed that neither the mesh size nor the baseline flow angle influence the flow sensitivities with respect to the parameters significantly on this particular configuration. The only consequence of this choice is then a small offset in the value of the C_L and C_D coefficients. For this configuration, the lift and drag coefficient are 1.92 and 0.04 respectively. These values are respectively on the lower and upper ranges of previous experimental and numerical predictions summarized by [2].

3.2 Sensitivity study

3.2.1 Single parameter analysis

It is worth studying the influence of each parameter on the lift and drag objectives. Using the first two derivatives for each parameter, the flow-field is extrapolated from the baseline configuration to compute the lift and drag forces. The resulting sensitivities are presented in fig. 7. Although the different parameters have different variation ranges Δp_{max}, this analysis reveals that some are more critical than others for the optimization. As a matter of fact, the flap rotation is the most effective parameter on the lift C_L coefficient, and one of the most effective on the drag, with both drag and lift increasing for decreasing angles (i.e. flap going vertical). This is actually expected since this parameter controls the overall camber of the high-lift device strongly and thus its lift and drag. More surprisingly, the slat rotation does not modify the lift and drag significantly. Aligning the slat with the airfoil (low angles) reduces the lift but increases the drag. The flow angle and the Mach number are also effective on both drag and lift levels. Drag and lift coefficients increase with Mach number and flow angle. The different translation parameters seem to act only slightly on the lift, some being even close to the optimum like the flap x-translation. On the contrary, these parameters are more effective on the drag coefficient, particularly the slat y-translation. The latter seems optimum on the baseline configuration.

For an airfoil and more specifically for a high-lift device, the sensitivity to flow angle is an important data. The lift and drag polar calculated parametrically here are plotted in fig. 8 with the envelope of the numerical and experimental data compiled by [2]. The reconstruction order is also studied in fig. 8 : the "1st order reconstruction" is based only on the first derivative with respect to the flow angle α; the "2nd order reconstruction" uses both the first and second order derivatives. First, the parameterization technique with the second order reconstruction is able to predict the variations of C_L and C_D coefficients fairly accurately. Although some difference in level remains, which might be caused by the use of the 11 c mesh with the standard flow angle, the slopes are correct for both coefficients. Secondly, the reconstruction order in fig. 8 is important. Unlike the lift coefficient prediction, which is quite insensitive to the order, the drag is largely over estimated by the first order reconstruction. This shows that the phenomena linked to the drag variations are mostly dependent on second- and higher order terms of the flow angle.

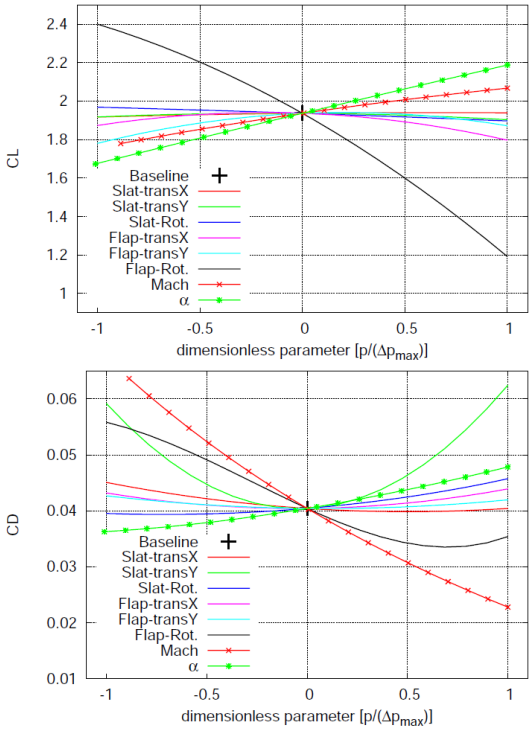

Fig. 7 Effects of parameters on lift and drag

3.2.2 Parameter coupling

Some interesting information on parameter coupling is available through the influence of cross-derivatives. These derivatives naturally account for the simultaneous influence of two parameters on the flow-field. Some two-parameter reconstruction using cross derivatives are represented in fig. 9, along with surface reconstructed without the cross-derivatives. The differences between the two kinds of surfaces are directly representative of the coupling effects. The analysis of the surfaces reconstructed for the two slat trans-

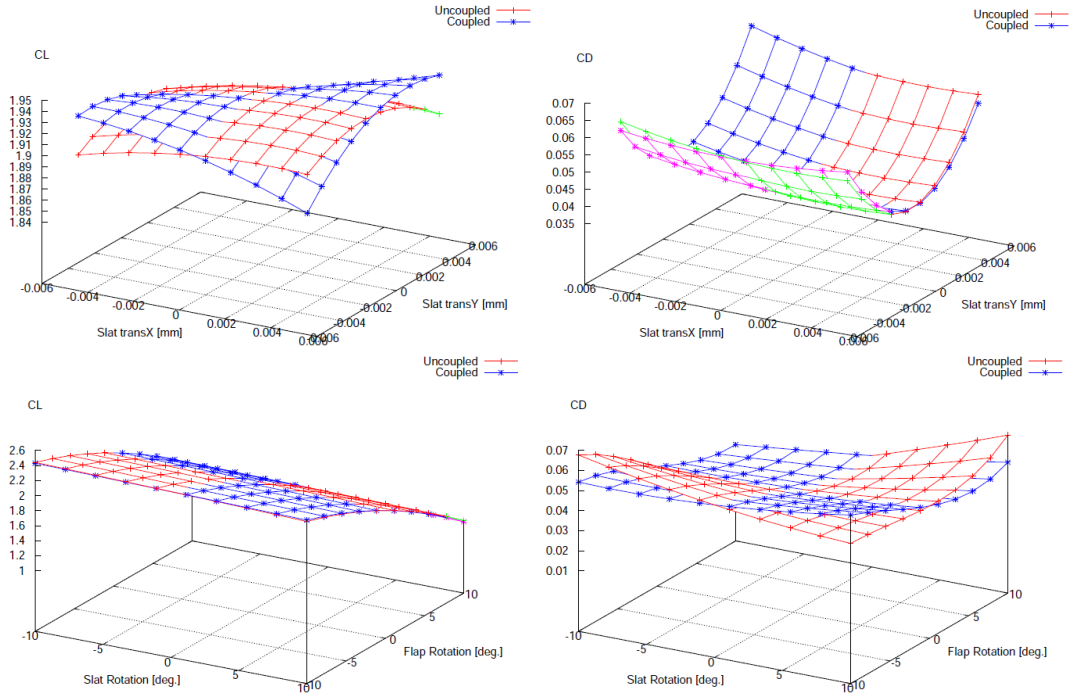

Fig. 9 Coupling effect between slat translation along x and y (top) and between the slat and flap rotations (bottom)

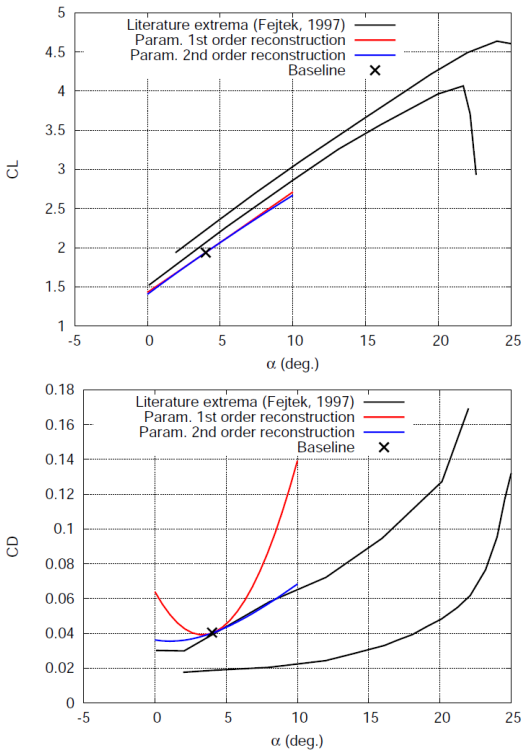

Fig. 8 L1T2 polar

lation (fig. 9 top) reveals that there is a strong coupling between the two parameters acting essentially on the lift. This coupling decreases the lift coefficient when the slat is moved simultaneously toward the main airfoil in the x and y directions. This is actually expected since this movement closes the gap at the end of the slat cove, reducing the possible re-energetisation of the airfoil suction-side flow. The coupling effect of these two parameters on the drag is much weaker, with a slight drag increase for a closer slat. Results are different when considering the slat and flap rotation coupling (fig. 9 bottom). The simultaneous rotation of each element has a negligible coupling effect on lift, as illustrated by the quasi-identical surfaces, but, it yields an important increase of the drag if both elements are turned toward the bottom. This suggests that the flow variation induced by the slat rotation have a weak effect on the main airfoil and flap lifts (confirmed by the single-parameter analysis in fig. 7) , but the same flow variation has some major effect of the flap drag: a flow analysis reveals that in this case, the flow over the flap suction side

is more likely to separate because of a slightly weaker flow coming from the airfoil suction side.

Using the same kind of analysis for every parameter couple, the slat parameters are found to have only minimal coupling with the flap parameters, except for the slat and flap rotations. The flow angle α is strongly coupled to the slat or flap rotation for drag: for instance, drag logically increases when slat and inlet flow angle diverge, or when the flap is down at high incidence. The Mach number has also a noticeable coupling with the rotation parameters: the slat in a down position and a high Mach number increase the drag.

3.2.3 Turbulence influence on parameterization

There are actually two distinct ways to treat the turbulent field with parameterization. On the one hand, derivatives of turbulent variables can be computed. This is the most obvious way to proceed. On the other hand, it is also possible to use a frozen turbulence hypothesis. This choice often comes for very difficult cases for which the turbulent flow-field can hardly be differentiated. The comparison of the two techniques provides a clear insight on the influence of turbulence on the overall flow. For this study, both parameterization where performed, and the corresponding variation for the most sensitive parameters are shown in fig. 10. The effects of turbulence in the present parameterization are diverse. For all the translations and the slat rotation, the frozen turbulence hypothesis induces a slight over-estimate of the lift for any parameter value. The most striking effect is for the flap rotation where frozen turbulence strongly under-estimates the lift for a flap in a down position. This is actually caused by a significantly wrong prediction of the flow features over the flap suction side, consistent with the arbitrary invariability of the turbulent field in this region. For the drag coefficient, the effects of the frozen hypothesis are the same for all parameters: it yields an underprediction of the drag that can be interpreted as neglecting the dissipation and losses induced by turbulence. The most sensitive parameter here is the y-translation of the slat that strongly affects the development of the airfoil boundary layer.

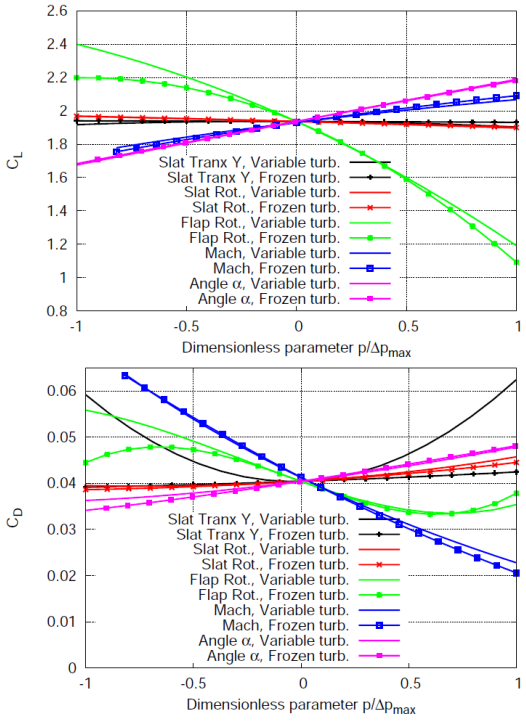

Fig. 10 Turbulence influence on parameterization

4 Optimization of the L1T2 high-lift device

The L1T2 high-lift device is optimized using the previous parameterization. The objectives are to increase the lift coefficient and decrease the drag coefficient. Two optimizations have been performed. The first one only takes into account the geometrical parameters (slat and flap translation rotations) and will be thereafter denoted as *geometrical optimization*, whereas the second one uses both geometrical and physical parameters (Mach number and flow angle) and is called *total optimization*. In both cases, the population reaches the Pareto front in approximately 20 generations and starts spreading over the front at this point.

The resulting Pareto fronts are presented in fig. 11. Both optimizations are effective since they povide an improvement with respect to the baseline configuration represented by the large black spots. There is nevertheless a clear difference between the results of geometrical and total optimizations. The total optimization yields

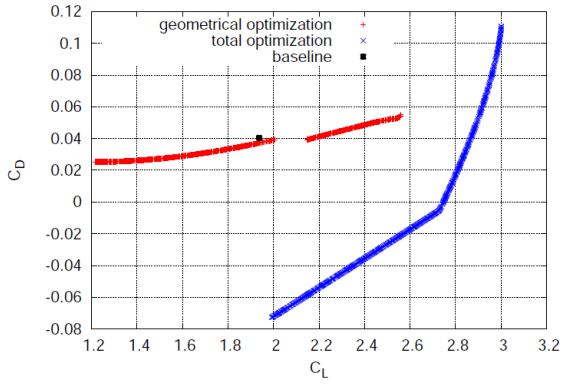

Fig. 11 Pareto fronts

Config.	Geom. Opt.		Total Opt.	
	C_L	C_D	C_L	C_D
iso-C_D	2.18	4.04e-02	2.87	4.04e-02
iso-C_L	1.93	3.69e-02	2.00	-7.2e-02
max-C_L	2.56	5.52e-02	3.00	11.1e-02

Table 3 Particular optimized configurations

broader variations relatively to the baseline configuration. The maximum lift achieved using all parameters is much higher than the one found using only geometrical parameter. The drag is also clearly reduced by the total optimization, though this optimization also yields a negative drag coefficient that is thought to be a consequence of the truncation error. Despite the limitation in the parameter ranges introduced to reduce the truncation error, the addition of this small residual error for each parameter is enough to create this negative drag. As a matter of fact, the trend observed here is correct (drag reduction), but the amplitude is over-estimated. The differences are further quantified in tab. 3 using three particular configurations noted *iso-*C_D, *iso-*C_L and *max-*C_L and characterized respectively by the same drag coefficient as the baseline, the same lift coefficient as the baseline and the maximum lift coefficient over the Pareto front. The topology of the Pareto fronts is also slightly different, the geometrical optimization presenting a discontinuity.

The difference between the two fronts is generated by the two flow parameters. The analysis of the parameter value on the Pareto front resulting from total optimization is achieved using SOM (fig. 12). The maps presented here share the same topology, one point of the map representing one individual on the Pareto front. The only difference between the maps is the colormap representing one dimension of the front (parameter or objective) for each map.

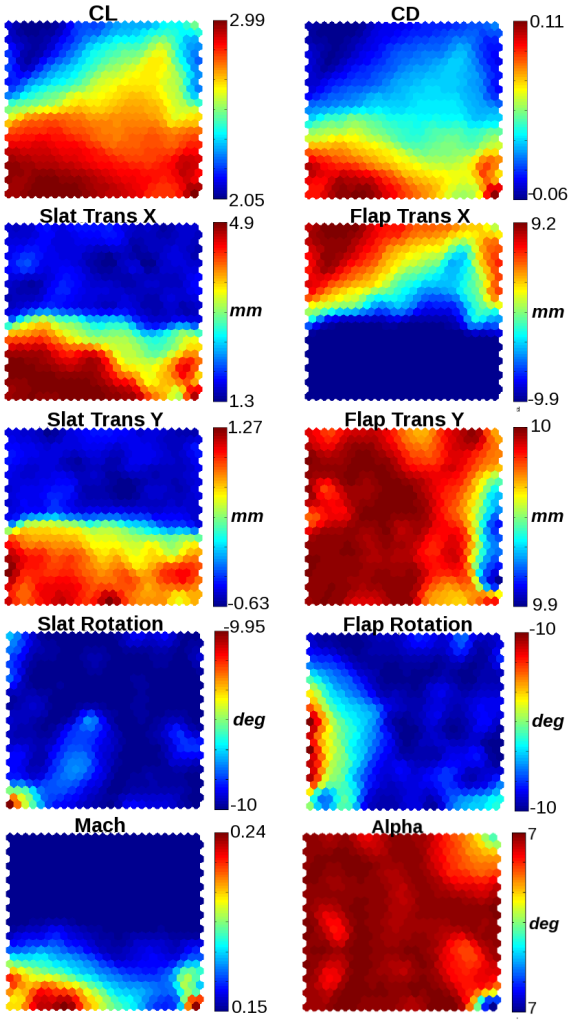

Fig. 12 SOM analysis - total opimization

The SOM reveals that on the Pareto front, all the configurations have the same slat and flap angles (slat up and flap down), set to their maximum value allowed here. This suggests that the optimization could be extended by shifting the baseline toward these values and optimizing again. This also confirms that the two rotations are critical parameters for lift and drag variations. The flow angle and the flap translation along y follow the same trend, being set to their maxima. The variation of the other parameters are larger. High

Mach numbers trigger high lift (and high-drag) configurations, whereas a low Mach number is favourable for drag reduction. The horizontal flap translation helps reducting the drag when moving the flap away from the airfoil: the obstruction at the flap-cove exit section decreases, but this also yields a lift reduction. The slat position is more complex. Lift is increased when moving the slat up and downstream along the airfoil suction side. The same analysis was performed for

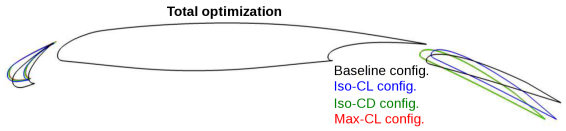

Fig. 13 L1T2 optimized configurations

the geometrical optimization (not shown here). It reveals that the geometrical parameters have approximately the same topology, which suggests that the coupling effects between the flow parameters and the geometrical ones have no major influence on the positioning optimization. The only noticeable difference is the flap rotation for the iso-C_L configuration that is very close to the baseline for the geometrical optimization. The iso-C_L, iso-C_D and max-C_L configurations are illustrated in fig. 13 for the total optimization. As it can be seen, the max-C_L and iso-C_D configurations are almost identical, which confirms the major part played by the Mach number in increasing the lift.

5 Conclusion

The L1T2 high-lift device was parameterized using both geometrical parameters controlling the position of the slat and the flap relatively to the main airfoil and physical parameters such as the flight Mach number of the flow angle. Numerical simulations showed the importance of the mesh size for such a configuration with important potential effects. A flow sensitivity analysis was performed using flow derivatives that revealed the relative influence of each parameter on the lift and drag, the coupling effect between the parameters and the importance of turbulence modelling for the optimization. The high-lift device has been optimized using a genetic algorithm using all parameters or only the geometrical ones.

As shown in this study, the optimization could be continued further by shifting the baseline toward the regions of interests. It would also be interesting to include new parameters such as the lift to drag ratio or the noise emission computed analytically. Finally, the present methodology could be applied to other high-lift devices and three-dimensional configurations.

References

[1] Moir, I.R.M., *Measurements on a two-dimensional aerofoil with high lift devices*. AGARD AR 303, vol IIn pp. A2.1-A2.12, 1994.

[2] Fejtek, T., *Summary of code validation results for a multiple element airfoil test case*. AIAA Paper 97-1932, 1997.

[3] Smati, L., Aubert, S., Ferrand, P., Massao, F. *Comparison of numerical schemes to investigate blade flutter*. 8th ISUAAT symposium, 1997.

[4] Moreau, S., Aubert, S., Grondin, G., Ferrand, P., *Optimisation of a fan blade cascade using the parametric flow solver Turb'Opty*. ASME Fluids Engineering Meeting, FEDSM2006-98543 2006.

[5] Deb, K., Agrawal, S., Pratap, A., Meyarivan, T., *A fast and elitist multi-objective genetic algorithm : NSGA-II*. IEEE Trans. Evol. Comput., 6(2), p 181-197 2002.

[6] Vesanto, J., Imberg, J., Alhomieni, E., Parhankangas, J., *SOM toolbox for Matlab5*. Helsinki University of Technology Tech. Rep. A57 2002.

Copyright Statement